Cellulose (2015) 22:2183–2195
DOI 10.1007/s10570-015-0638-7

ORIGINAL PAPER

Cellulose co-crystallization and related phenomena occurring in hydrothermal treatment of sugarcane bagasse

Carlos Driemeier · Fernanda M. Mendes · Beatriz S. Santucci · Maria T. B. Pimenta

Received: 9 December 2014 / Accepted: 16 April 2015 / Published online: 24 April 2015

Abstract Lateral dimensions of cellulose crystallites have been widely reported to increase as plant biomasses are submitted to a variety of high-temperature chemical treatments. Cellulose co-crystallization is often indicated to be the phenomenon underlying crystallite dimensional change, but precise mechanisms and relationships with concurrent phenomena are not well understood. This work investigates cellulose structural evolution in sugarcane bagasse submitted to wide range (160–190 °C, up to ≈50 % solubilization) of hydrothermal treatments, performed in pressurized liquid hot water. Cellulose structural characterization combines fiber and powder X-ray diffraction with analysis of two-dimensional diffraction patterns employing the Cellulose Rietveld Analysis for Fine Structure (CRAFS) model. We observe that increases in lateral dimensions of cellulose crystallites closely follow changes in bagasse chemical composition. For a given composition, treatment temperature *per se* seems to be secondary for changes in crystallites. Partial cellulose de-crystallization and decreasing distortion of crystallite unit cell are found to co-occur with increasing crystallite lateral dimensions. Our interpretation of results emphasizes the importance of removing hemicelluloses acting as intercrystallite spacers, which seems to be the limiting factor for cellulose co-crystallization.

Keywords Cellulose · Crystallinity · Diffraction · Co-crystallization · Pretreatment · Sugarcane

C. Driemeier (✉) · F. M. Mendes · B. S. Santucci · M. T. B. Pimenta
Laboratório Nacional de Ciência e Tecnologia do Bioetanol – CTBE/CNPEM, Rua Giuseppe Máximo Scolfaro, 10.000, CP 6170, Campinas, São Paulo 13083-970, Brazil
e-mail: carlos.driemeier@bioetanol.org.br

B. S. Santucci
Instituto de Química de São Carlos – Universidade de São Paulo, Avenida Trabalhador São-carlense, 400, CP 780, São Carlos, São Paulo 13560-970, Brazil

Introduction

Lignocellulosic biomass has attracted considerable research effort in recent years because this type of biomass is a vast renewable resource that can be industrially converted into value-added materials, chemicals, and liquid biofuels. Chemical fractionation is one common step of biomass conversion routes. For instance, several types of fractionation have been developed as pre-treatments performed prior to enzymatic saccharification for production of second-generation bioethanol (Mosier et al. 2005; Alvira et al. 2010; Wyman 2013). Hydrothermal treatments are arguably the simplest type of biomass chemical fractionation since treatment inputs comprise only biomass, heat, and liquid water. This simplicity has been appealing from economic, environmental, and basic research perspectives. Performed in pressurized

liquid hot water (at 150–220 °C), hydrothermal treatments hydrolyze and solubilize preferentially the hemicellulosic fraction of the biomass, producing solids enriched in cellulose (Garrote et al. 1999; Ruiz et al. 2013).

Although the objectives of biomass chemical fractionation are often expressed in terms of compositional changes, treatments also alter biomass structure at several length scales (Cheng et al. 2014; Inouye et al. 2014; Nishiyama et al. 2014). In particular, change in cellulose crystallites has been observed as decreasing width of equatorial X-ray diffraction (XRD) peaks, namely the (1-10), (110), and (200) peaks indexed according to the cellulose Iβ crystal structure (Nishiyama et al. 2002; French 2014). Such sharpening of XRD peaks has been reported by several research groups investigating various biomasses, treatment types, and treatment conditions (Ioelovitch 1992; Leppänen et al. 2009; Sun et al. 2014a), including treatments in either vapor or liquid water (Inagaki et al. 2010; Driemeier et al. 2011; Penttilä et al. 2013; Langan et al. 2014; Nishiyama et al. 2014). In addition to such XRD observations, solid-state ^{13}C nuclear magnetic resonance (Newman 1999; Foston and Ragauskas 2010; Sun et al. 2014a) and small-angle neutron scattering (Langan et al. 2014; Pingali et al. 2014) have provided evidence most likely reflecting the same cellulose restructuring that generates sharper XRD peaks. This set of results has been interpreted primarily as treatment-induced increase in lateral dimensions of cellulose crystallites and *co-crystallization* is often, but not always, proposed as the mechanism promoting such crystallite widening. Later in this article, more precise definition of co-crystallization will be given and uncertainties in interpretation of experimental data will be discussed. Nevertheless, for the sake of this introduction, it should be clear that the abundance of evidence collected from a broad range of biomass types and treatment conditions demonstrates that cellulose crystallites are restructured during several types of lignocellulose chemical fractionation processes, including hydrothermal treatments.

In this work, we refine current understanding of such cellulose structural evolution. Concretely, we investigate the effects of hydrothermal treatments applied to sugarcane bagasse, the lignocellulosic residue produced by industrial crushing of sugarcane stalks (Cortez 2010). We employ XRD to characterize cellulose crystallites in raw and treated sugarcane bagasse. Accuracy and precision of XRD analysis are enhanced by a combination of fiber and powder diffraction modes and analysis of two-dimensional XRD patterns employing the model Cellulose Rietveld Analysis for Fine Structure (CRAFS) (Oliveira and Driemeier 2013; Driemeier 2014). Furthermore, cellulose structural parameters are determined as function of processing conditions and composition changes, informing on phenomena co-occurring with structural modifications of cellulose crystallites.

Materials and methods

Sugarcane bagasse

Sugarcane bagasse was collected at the end of the bagasse conveyor belt from Usina de Açúcar e Álcool São José, Rio das Pedras, São Paulo, Brazil. Bagasse was initially air-dried for storage. Representative sample of this bagasse was fractioned in a vibratory sieving column (Analysette 3, Fritsch GmbH) assembled with six sieves (mesh openings of 4.0, 1.18, 0.85, 0.60, 0.425, and 0.250 mm). The coarser fraction (retained at the 4.0 mm sieve) as well as fines rich in bagasse pith (fractions passed through the column and retained at the bottom 0.250 mm sieve) were discarded. The remaining fractions, made primarily of fibrous particles, were mixed, homogenized, and extensively rinsed in water to remove residues of sand, pith, and sucrose. The resulting washed depithed sugarcane bagasse, henceforth termed simply as *bagasse*, was used in the following experimental steps.

Hydrothermal treatments

Hydrothermal treatments were performed in custom-built 316L stainless steel batch reactors of 200 mL capacity. For each treatment, reactors were filled with 12 g (dry basis) of bagasse plus distilled water to establish liquid-to-solid ratio of 10:1. Reactors were heated in a glycerin bath calibrated to perform reactions at 160, 170, 180, and 190 °C. Effective treatment times ranged from 2.5 to 90 min, with effective treatment time defined as residence time (at target temperature) plus corrective time due to heating ramp. [Corrective time multiplied by target temperature was made equal to the integral of calibrated

heating curve (temperature × time), starting at 100 °C.] Corrective times were in the range of 12–22 min. Hence, target temperatures were not completely reached for effective treatment times shorter than that. Reactions were finished by quenching reactors in an ice bath. Reaction products were filtered in a custom-made polyester mesh, with negligible loss of fines. Solid reaction products were separated by filtration and were extensively rinsed in water ($\approx$16 L of water per treatment) to remove soluble residues impregnated in the solids.

Determination of solubilization and chemical composition

Solubilization was defined as the mass percentage (dry-basis) leaving the solid phase due to hydrothermal treatments. Solubilization was determined gravimetrically by analysis of reactor solid mass input and output. Dry masses of initial and treated solids were determined from wet masses corrected for their respective moisture contents, which were evaluated by means of a thermobalance (model MA35, Sartorius).

Chemical composition of solids was determined through standard two-step analytical sulfuric acid hydrolysis (Sluiter et al. 2008). Insoluble lignin was determined gravimetrically as the acid-insoluble residue subtracted of its ash content. Soluble lignin, cellulose, and hemicelluloses were quantified from analyses of acid hydrolysis filtrate. Soluble lignin was determined from ultraviolet absorbance in 280 nm, as described by Gouveia et al. (2009). Cellulose content was calculated from concentrations of cellobiose, glucose, hydroxymethylfurfural, formic acid, and glucuronic acid measured by high performance liquid chromatography (HPLC). Content of hemicelluloses was calculated from concentrations of xylose, arabinose, furfural, and acetic acid, also measured by HPLC. Ash content was determined gravimetrically from the residue of dry oxidation, following the procedure of Sluiter et al. (2005). Lignin content was reported as total lignin (soluble plus insoluble). Chemical composition of untreated bagasse was determined with an additional step (performed prior to analytical acid hydrolysis) for removing organic compounds of low molecular weight (extractives). This step was not required for treated bagasse because of their negligible content of extractives. Extraction was done with cyclohexane/ethanol (1:1, v:v) and water, following TAPPI method T204 cm-97 'Solvent Extractives of Wood and Pulp'. All contents were reported as dry-basis mass fractions, in units of g/g.

Fiber and powder X-ray diffraction

X-ray fiber diffraction was performed with air-dried single bagasse particles aligned perpendicularly to the X-ray beam and rotated around the particle axis during X-ray exposure in transmission mode. The fibrous particles were several millimeters long and a few hundreds of microns in diameter, consisting mainly of fragments of aggregated vascular bundles from sugarcane stalks. Selection of particles for fiber diffraction was a biased process because more robust particles were easier to handle and thus preferred to smaller, mechanically weaker ones. Despite this bias in sampling, fiber diffraction had the advantage of generating more informative diffraction patterns due to azimuthal resolution of diffraction peaks. Powder diffraction, on the other hand, was conducted with air-dried fibrous particulates conditioned in capillary tubes (Charles Supper special glass, 2 mm diameter). The capillary tubes were aligned and rotated as in single-particle fiber diffraction. In this powder diffraction setup, azimuthal resolution of diffraction peaks was diminished due to particle disorientation within the capillary tube, but analyzed samples were representative of bagasse particulates. Reported results of powder diffraction were typically the average of duplicate analysis. With all considered, combining fiber and powder diffraction brought complementary advantages to the XRD analysis: better resolution in fiber diffraction and better representativeness in powder diffraction.

Fiber diffraction was performed at the MX1 beamline of the Brazilian Synchrotron Light Laboratory (Polikarpov et al. 1998), with X-ray wavelength $\lambda = 1.4535$ Å. Powder diffraction was performed in a Rigaku ultraX-18HF rotating anode generator with Cu$K\alpha$ radiation ($\lambda = 1.5418$ Å) and VariMax HR monochromating optics. Both fiber and powder diffraction used the same X-ray detection setup, with a mar345 image plate to collect diffraction patterns and a Xenocs PIN diode to monitor X-ray transmission through samples. Instrumental line broadening and scattering angle 2θ were calibrated with an α-alumina reference sample. Prior to diffraction pattern analysis,

geometric, polarization and absorption corrections were applied to X-ray intensities (Driemeier and Calligaris 2011; Oliveira and Driemeier 2013).

Two-dimensional X-ray diffraction patterns were analyzed by the Rietveld method using the CRAFS model (Oliveira and Driemeier 2013; Driemeier 2014). CRAFS analysis fitted calculated XRD patterns to experimental ones. The automated fitting procedure determined CRAFS parameters for crystallite unit cell, crystallite size, diffraction peak shape, crystalline signal intensity, polynomial background intensity, and crystallite orientation distribution. CRAFS parameters L_δ and p_δ were set equal to zero, which implies the (1-10) and (110) diffraction peaks having identical width and shape. CRAFS Gaussian contribution to crystallite orientation distribution function was equaled to zero in analysis of powder patterns because this contribution is only relevant for fiber diffraction. For reasons detailed in "Results", CRAFS peak shape parameters p_{200}, p_{diag} ($p_{diag} = p_{1\bar{1}0} = p_{110}$), and p_{004} were free in analyses of fiber diffraction, whereas they were fixed ($p_{200} = 0.75$, $p_{diag} = 0.50$, and $p_{004} = 0.75$) for analyses of powder diffraction.

Specimen degree of crystallinity x_{cr}, defined as g cellulose crystal per g dry specimen, was determined from powder diffraction patterns following the developments of Driemeier and Calligaris (2011),

$$x_{cr} = \frac{Q_{cr}}{Q_{\exp} - (T_{\exp}/T_0)Q_0} \times \frac{1 + 1.2x_m - 0.1x_l + 0.74x_{ash}}{1 - \varepsilon_{inc}} \quad (1)$$

In Eq. 1, Q_{cr}, Q_{exp}, and Q_0 are integrals of, respectively, coherent crystalline intensity in CRAFS isotropic reconstruction of experimental XRD pattern, total intensity in CRAFS isotropic reconstruction, and blank intensity acquired from exposures of empty capillary tubes. T_{exp} and T_0 are transmitted X-ray intensities during specimen and empty tube exposures, respectively. The factor to the right-hand side of '×' corresponds to corrective parameters. ε_{inc} accounts for incoherent scattering (0.1 for Cu$K\alpha$), x_m is specimen dry-basis moisture content (determined with thermobalance), x_l is lignin content and x_{ash} is ash content. The corrective coefficients associated with lignin and ash contents (−0.1 and 0.74, respectively) were calculated in Driemeier et al. (2011).

Precision in x_{cr} is critically influenced by uncertainty in blank subtraction [the term $(T_{exp}/T_0)Q_0$ in Eq. 1] and this uncertainty is propagated for estimating x_{cr} error bars. For the other XRD parameters, dispersion of data points within observed trends provides adequate estimates of measurement precisions.

Results

Solubilization and composition

Hydrothermal treatments solubilize fractions of bagasse. Figure 1 shows dry-mass percentages solubilized by the treatments as function of effective treatment time, for treatments performed at 160, 170, 180, and 190 °C. A clear and expected trend of increasing solubilization with increasing time and temperature is evidenced. Rate of solubilization progressively decreases as treatment proceeds in time, which is due to progressive consumption of components (primarily hemicelluloses) that are preferentially solubilized under treatment conditions (Garrote et al. 1999; Ruiz et al. 2013).

Composition of raw and hydrothermally treated solids is presented in Fig. 2. Contents of cellulose, hemicelluloses, and lignin are presented as function of solubilization, which collapse data points from different temperatures into a common trend. As solubilization proceeds, contents of cellulose progressively increase (from 0.43 to 0.71 g/g), whereas of hemicelluloses decrease (from 0.30 to 0.03 g/g). Lignin contents increase only marginally (from 0.23 to

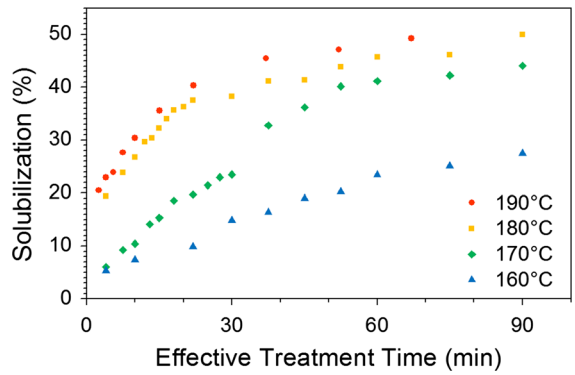

Fig. 1 Solubilization due to hydrothermal treatments as function of effective treatment time

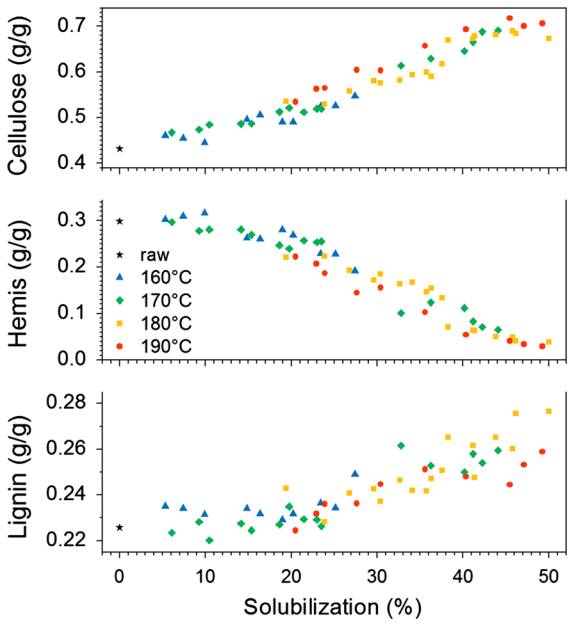

Fig. 2 Chemical composition of raw and treated bagasse. Contents of cellulose, hemicelluloses, and total lignin are presented as function of solubilization

0.28 g/g). From solubilization and composition of treated solids, we calculate that treatments solubilized up to ≈22 % (at most severe condition) from *cellulose* of raw bagasse. Furthermore, for a given solubilization, chemical composition is generally independent of treatment temperature. Treatments at 190 °C seem to be an exception to this rule because for this temperature contents of cellulose (hemicelluloses) are slightly but consistently above (below) the common trend of composition against solubilization (Fig. 2).

CRAFS analysis of two-dimensional diffraction patterns

Figure 3 presents examples of XRD patterns and their analysis with CRAFS. Figure 3a–c exemplify single particle fiber diffraction. Figure 3a presents the raw XRD pattern, evidencing the azimuthal resolution of XRD peaks typical of cellulose I fiber diffraction. Figure 3b presents the corrected two-dimensional experimental pattern and its fit and residue from CRAFS analysis. It shows that main features of experimental data are well represented by the model, although some misfits are shown by the residue pattern. Figure 3c presents the experimental and modelled components of the diffractogram from an equatorial slice (azimuthal angle $\eta = 90°$) of the two-dimensional pattern. One observes relatively minor misfits to the most intense diffraction peaks. Powder diffraction of particulates in capillary tubes is exemplified in Figs. 3d–f. Diffraction rings typical of powder diffraction are observed in the raw two-dimensional pattern of Fig. 3d. Variable intensity along the rings evidences some preferential crystallite orientation. Fitting with CRAFS reproduces most features of the experimental two-dimensional pattern (Fig. 3e). The major misfit (at $2\theta \approx 31°$) in diffractogram of Fig. 3f is due to stacking faults (mixed Iα–Iβ stacking) in cellulose crystallites, as proposed by Driemeier and Francisco (2014). This type of crystallographic defect is not considered in CRAFS (Oliveira and Driemeier 2013), which is based on the Iβ crystal structure (Nishiyama et al. 2002). Furthermore, the substantial intensity of the polynomial background (Fig. 3f) is in large part due to scattering from the capillary tube containing the bagasse particulate, which is properly accounted for in determination of degree of crystallinity (see Eq. 1).

Diffraction peak profiles

CRAFS calculates diffraction peaks with pseudo-Voigt functions that are a sum of Gaussian and Lorentzian components. Peak shape parameter p weights both contributions, varying from $p = 0$ (Gaussian) to $p = 1$ (Lorentzian). By increasing p, peak profiles gain more Lorentzian character, which implies more intensity attributed to far-reaching peak tails. Concretely, the applied CRAFS analysis has three distinct p parameters: p_{200} for (200) peak; p_{diag} for (1–10) and (110) peaks; and p_{004} for (004) peak. Profile parameters for all the other XRD peaks are estimated from p_{200}, p_{diag}, and p_{004} (Oliveira and Driemeier 2013). Although CRAFS is designed to allow determination of p_{200}, p_{diag}, and p_{004} through least-square fit of experimental data, analysis of *powder patterns* produced erratic outputs for p parameters. We observed neither consistency within replicated experimental patterns nor trends as a function of hydrothermal treatment conditions. From this observation, we concluded that bagasse powder patterns have insufficient resolution to reliably inform about peak shape parameters, which justified usage of

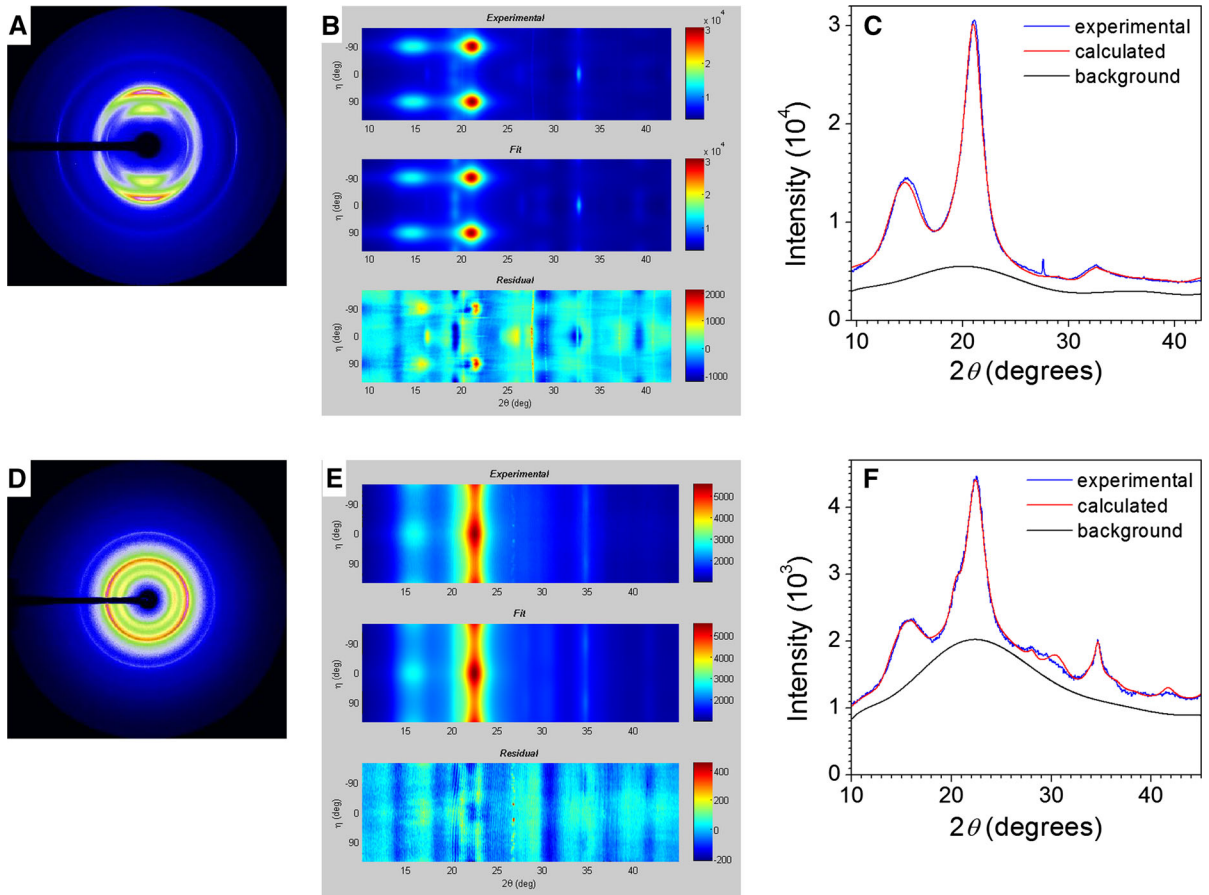

Fig. 3 Examples of two-dimensional diffraction patterns acquired in **a**–**c** fiber and **d**–**f** powder diffraction modes. Presented patterns were acquired from bagasse treated at 190 °C with ≈45 % solubilization. **a**, **d** Raw experimental patterns. **b**, **e** Corrected two-dimensional experimental patterns, presented in rectangular coordinates with fits and residues from CRAFS analysis. **c**, **f** Equatorial ($\eta = 90°$) slices from two-dimensional patterns, showing experimental and calculated intensities as well as intensity from isotropic polynomial background. Differences between 2θ scales are due to different X-ray wavelengths: **a**–**c** $\lambda = 1.4535$ Å and **d**–**f** $\lambda = 1.5418$ Å

fixed peak shape parameters in analysis of powder patterns (see section "Methods").

In single particle fiber diffraction, on the other hand, consistency in peak shape parameters was obtained from CRAFS analysis. Parameter p_{200} increases as function of solubilization, from $p_{200} \approx 0.76$ for raw bagasse to $p_{200} \approx 0.88$ for solid treated to 45 % solubilization (Fig. 4). Parameter p_{diag} does not present any clear trend as function of solubilization, but p_{diag} is consistently below p_{200} (Fig. 4). Higher Lorentzian character (*i.e.*, higher p) may arise from greater variability of crystallite sizes along a given crystallographic direction (Oliveira and Driemeier 2013). Thus, p_{200} increasing with solubilization is consistent with the statistical nature of increasing crystallite lateral dimensions, with some crystallites being more affected than others. Furthermore, $p_{200} > p_{diag}$ is consistent with preferential exposure of hydrophilic {1-10} and {110} facets of cellulose crystallites, which results in greater size variability along [200] direction (Oliveira and Driemeier 2013). Higher Lorentzian character may also arise from states of order intermediate between crystalline and isotropic amorphous. Other authors employed dedicated broad peaks to represent such intermediate orders (Thomas et al. 2013; Nishiyama et al. 2014). However, CRAFS considers only oriented crystals and isotropic amorphous components so that

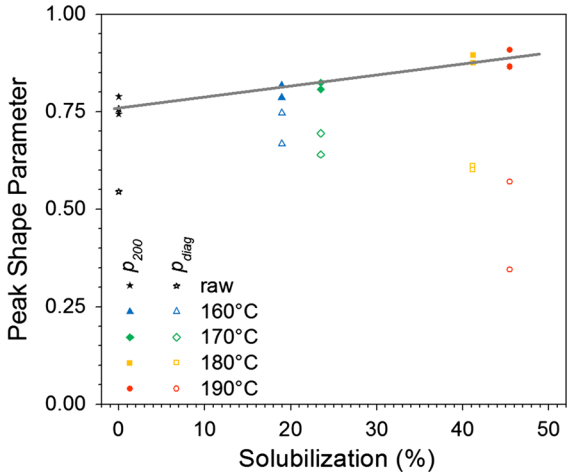

Fig. 4 Peak shape parameters p_{200} and $p_{diag} = p_{1\bar{1}0} = p_{110}$ obtained from CRAFS analysis of single-particle fiber patterns. The *gray line* guides the eye through the trend of p_{200} increasing with solubilization

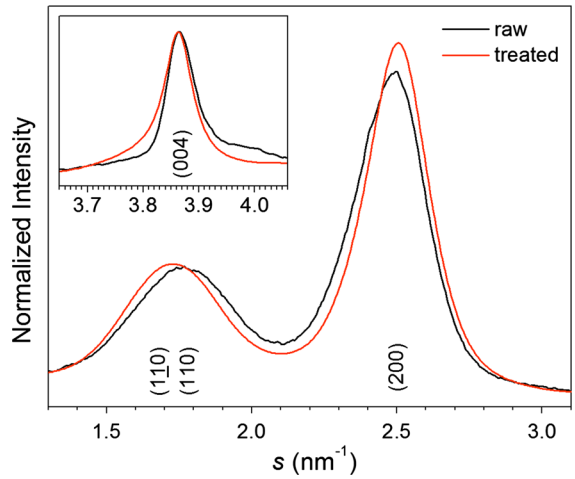

Fig. 5 X-ray diffraction diagrams acquired in fiber diffraction mode from single particles of raw and treated (190 °C, 45 % solubilization) bagasse. The *main graph* and the *inset* show, respectively, equatorial ($\eta = 90°$) and meridional ($\eta = 0°$) slices of area-detector patterns. Presented intensities are subtracted of isotropic polynomial background (resolved by CRAFS) and normalized either to unit area (*main graph*) or to unit maximum (*inset*). Main (*hkl*) reflections are identified. Diagrams are presented as function of $s = 2\sin(\theta)/\lambda$

intermediate orders may be partly represented by the far reaching tails from Lorentzian components of diffraction peaks (Oliveira and Driemeier 2013; Driemeier 2014).

For analysis of powder patterns, the employed peak shape parameters ($p_{200} = 0.75$, $p_{diag} = 0.50$, and $p_{004} = 0.75$) are close to those obtained from fiber diffraction of bagasse (Fig. 4). In addition, similar peak shape parameters were determined in fiber diffraction of Arabidopsis stems and Eucalyptus wood (to be reported in forthcoming publications). Importantly, the choice of peak shape parameters, especially p_{200}, significantly influences the accuracy of x_{cr} (Oliveira and Driemeier 2013), as further discussed in section "Degree of crystallinity". Fixed peak shape parameters, however, allow changes in experimental patterns to be systematically reflected by the other model parameters (see below), without detrimental interference from unjustified variations in peak profile functions (Oliveira and Driemeier 2013). Therefore, usage of such fixed peak shape parameters seems to be a valid and useful recommendation for CRAFS analysis of powder patterns from lignocellulosic biomasses.

Crystallite size and unit cell

The major changes observed between XRD diagrams of raw and treated bagasse are summarized in Fig. 5. As a first observation, equatorial diffraction peaks become sharper after bagasse treatment. This effect is more evident for relatively isolated (200) peak, while less clear for overlapped (1-10)/(110) peaks. As mentioned in the introduction, such sharpening of equatorial diffraction peaks has been abundantly reported (Ioelovitch 1992; Leppänen et al. 2009; Inagaki et al. 2010; Driemeier et al. 2011; Penttilä et al. 2013; Sun et al. 2014a; Langan et al. 2014; Nishiyama et al. 2014). In CRAFS, diffraction peak width has an inverse relation with crystallite size (Oliveira and Driemeier 2013), as in Scherrer equation (Langford and Wilson 1978). Therefore, sharper diffraction peaks are analyzed as larger crystallite dimensions. From analysis of powder patterns, lateral dimensions L_{200} and $L_{1\bar{1}0} = L_{110}$ increase progressively with solubilization (Fig. 6). In line with the observation for contents of cellulose and hemicelluloses (Fig. 2), different treatment temperatures belong to a common trend, perhaps with 190 °C as exception. Likewise for cellulose contents (Fig. 2), data for 190 °C is slightly but consistently above the trends of lateral dimensions (L_{200} and $L_{1\bar{1}0} = L_{110}$) as function of solubilization (Fig. 6). A scatter plot of L_{200} versus contents of hemicelluloses (top graph of Fig. 6) makes

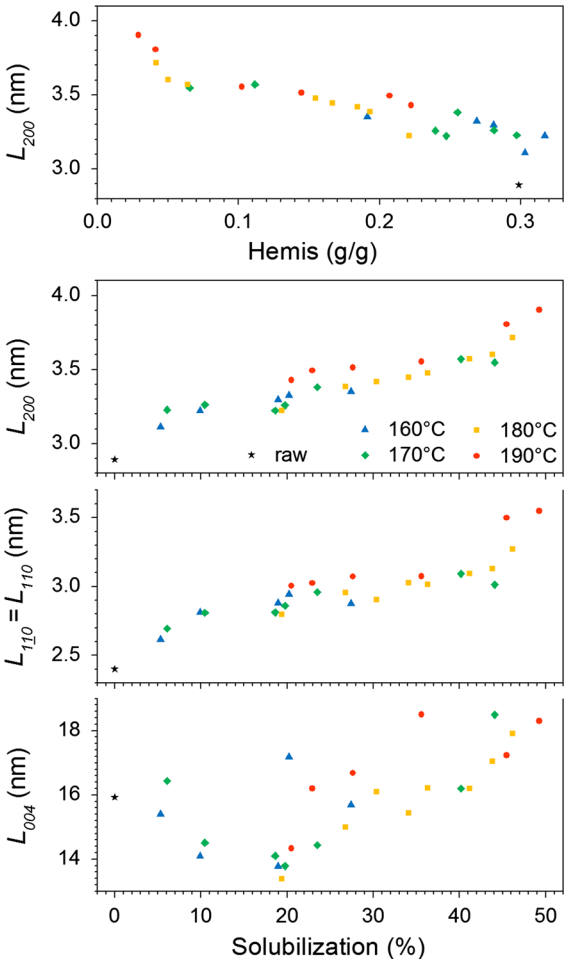

Fig. 6 Cellulose crystallite lateral dimensions (L_{200} and $L_{1\bar{1}0} = L_{110}$) and apparent crystallite length L_{004} obtained from CRAFS analysis of powder patterns. The crystallite size parameters are presented as function of solubilization, except for the *top graph*, which shows L_{200} against content of hemicelluloses

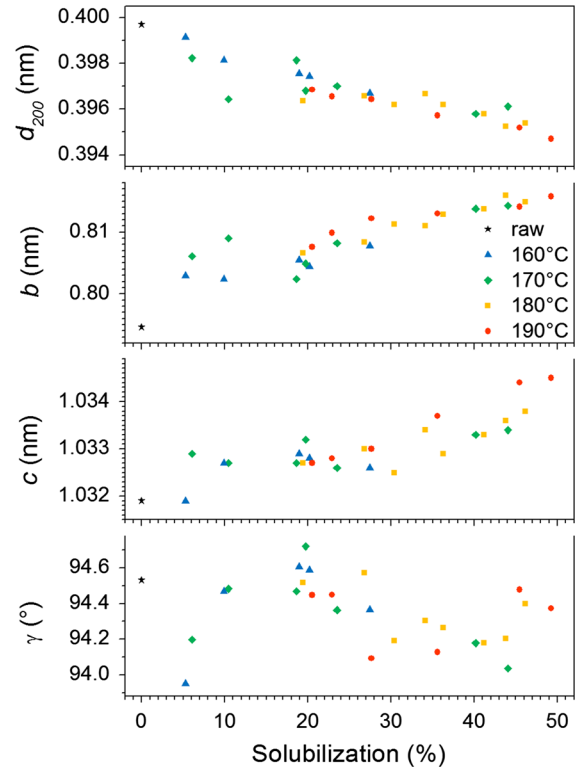

Fig. 7 Cellulose unit cell parameters obtained from CRAFS analysis of powder patterns presented as function of solubilization. Spacing $d_{200} = ½\ a\ \mathrm{sen}(\gamma)$ is presented instead of unit cell parameter a because d_{200} is directly related to the position of (200) diffraction peak

clear that crystallite lateral dimensions closely follow changes in bagasse composition. On the other hand, for a given composition, treatment temperature *per se* seems to be a factor of minor importance for increasing crystallite lateral dimensions. Furthermore, appreciable increase in lateral dimensions is already notice at low (≈5 %) solubilization, consistent with cellulose restructuring starting at early stages of treatment (Pingali et al. 2014). Differently from changes at higher solubilization, this early stage shows no concurrent decrease in content of hemicelluloses (Fig. 2).

Next, we observe the shifting of equatorial peaks (Fig. 5). CRAFS analysis of powder patterns reveals no clear trend for the monoclinic angle γ as function of solubilization (Fig. 7), with the remark that determination of γ is quite uncertain due to overlap between (1-10) and (110) peaks. On the other hand, analysis reveals d_{200} decreasing and unit cell parameter b increasing progressively with solubilization (Fig. 7). These changes in d_{200} and b are consistent with the directions of peak shifts observed in Fig. 5. Importantly, as solubilization increases, d_{200} and b approach reference values ($d_{200} = 0.387$ nm, $b = 0.820$ nm) from the cellulose Iβ crystal structure (Nishiyama et al. 2002). Approaching reference parameters indicates that distorted unit cell is a feature of raw sugarcane bagasse, with treatments acting to attenuate the native distortion. Noteworthy, native cellulose unit cell parameters depend on plant taxonomy (Okano and Koyanagi 1986) and distortion in

unit cell parameters seems to be especially pronounced in sugarcane cellulose (Driemeier et al. 2012). Therefore, the *magnitude* of treatment-induced changes in unit cell parameters may be specific of sugarcane bagasse. Nevertheless, the trend of approaching reference Iβ unit cell is likely general because hemicelluloses, which are removed by treatments, likely drive distortion, while larger crystallites, which are formed by treatments (Fig. 6), are less prone to distortion (Driemeier et al. 2011).

Considering meridional (004) peak, fiber diffraction reveals change in peak shape, with a right-hand peak tail observed for raw bagasse and a left-hand tail for treated bagasse (Fig. 5 inset). CRAFS is unable to analyze such peak asymmetry. However, reflecting the shift of peak centroid (see inset of Fig. 5), CRAFS analysis of powder patterns reveals fiber repeat c increasing with solubilization (Fig. 7), also approaching the reference value ($c = 1.038$ nm) from the Iβ crystal structure (Nishiyama et al. 2002). Noteworthy, combination of results from Figs. 6 and 7 shows c increasing with crystallite lateral dimensions (L_{200} and $L_{1\underline{1}0} = L_{110}$), which is the trend previously reported by Davidson et al. (2004). Crystallite length L_{004}, derived from width of (004) peaks, does not present any clear trend with solubilization (Fig. 6). Importantly, CRAFS tends to critically underestimate L_{004} because relevant contributions to (004) diffraction line broadening are not known clearly.

Degree of crystallinity

Specimen degree of crystallinity x_{cr} is plotted against cellulose content in Fig. 8. The diagonal line of zero intercept and unit slope corresponds to the ideal case where all cellulose, and only cellulose, contributes to crystalline signal. We observe that raw and mildly treated bagasses are consistent with the diagonal line. However, for more severe treatments (resulting in higher cellulose contents), x_{cr} becomes systematically below cellulose content. This difference between x_{cr} and cellulose content indicates presence of non-crystalline cellulose in treated bagasse, whereas raw bagasse is consistent with fully crystalline cellulose.

Peak profile functions employed in XRD modelling are known to affect estimates of x_{cr} because diffraction peak tails contribute to what is accounted as crystalline signal. In CRAFS, concretely, increasing p_{200} is known to increase estimates of x_{cr} (Oliveira and Driemeier 2013). Therefore, it is important to verify how results of Fig. 8 are modified by changing from $p_{200} = 0.75$ (see section "Methods") to p_{200} in better agreement with those values determined from fiber diffraction (Fig. 4). We recalculated x_{cr} of the five bagasse samples treated at highest severity (with cellulose >0.68 g/g). Values of x_{cr} increase ≈0.05 g/g by recalculation with $p_{200} = 0.90$, which would agree with p_{200} from fiber diffraction (Fig. 4). For the extreme case of $p_{200} = 1$, x_{cr} increase ≈0.08 g/g compared to results of Fig. 8. Such gains in x_{cr} are, however, insufficient to change the conclusion that a fraction of cellulose is de-crystallized at severe hydrothermal treatments. Noteworthy, this result is a refinement of our previous analysis (Driemeier et al. 2011) when our XRD modeling was unable to investigate variations in diffraction peak shape, which became a possibility with CRAFS (Oliveira and Driemeier 2013; Driemeier 2014).

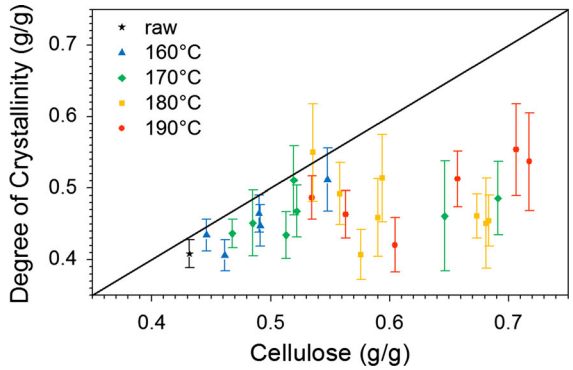

Fig. 8 Specimen degree of crystallinity obtained from CRAFS analysis of powder patterns plotted against cellulose content. Both variables are presented as mass fraction (g/g), having dry matter as denominator. *Diagonal line* has zero intercept and unit slope. *Error bars* are precisions (1σ) estimated from replicated measurements

Discussion

Definition and defense of cellulose co-crystallization

Cellulose co-crystallization is here defined as the formation of crystallites of larger lateral dimensions

resulting from interactions of *multiple* adjacent crystallites existing in the initial, raw state of the biomass.

The primary experimental observation supporting co-crystallization is the sharpening of equatorial XRD peaks (Fig. 5), parameterized by CRAFS as increasing L_{200}, $L_{1\bar{1}0}$, and L_{110} (Fig. 6). Given the precision of the our analysis as well as similar findings from several independent studies (Ioelovitch 1992; Leppänen et al. 2009; Inagaki et al. 2010; Driemeier et al. 2011; Penttilä et al. 2013; Sun et al. 2014a; Langan et al. 2014; Nishiyama et al. 2014), the observation of sharper equatorial XRD peaks after hydrothermal treatment is undisputable.

However, attributing sharper XRD peak to larger crystallite size is a matter of interpretation, where uncertainties remain. In addition to crystallite size, several types of crystallite imperfection may contribute to broadening of diffraction peaks. It is therefore important to estimate the magnitude of other line broadening contributions and then verify whether observed peak sharpening is beyond such uncertainty level. With this objective we note that, in polymers, defects of the second kind, which consist of statistical fluctuations in interplanar spacing, have been considered as the main type of line-broadening imperfection (Roe 2000). The impact of such imperfections on XRD line broadening has been explained by Hosemann paracrystallinity theory coupled to the empirical α^* relation (Hosemann and Hindeleh 1995). In this theoretical framework, smaller crystallites are also more imperfect because of their larger specific surface area. In quantitative terms, broadening due to Hosemann paracrystallinity is proportional to broadening due to size, merely changing the proportionality factor (shape factor) of the Scherrer equation. This correction for Hosemann paracrystallinity is encoded in CRAFS. For (200) peaks this correction corresponds to $\approx$19 % increase in the shape factor of the Scherrer equation (Oliveira and Driemeier 2013). Considering Hosemann paracrystallinity as the main type of line broadening imperfection for equatorial peaks, other broadening contributions are expected to be relatively minor, in round number limited to about 10 % of peak width. Such a percentage is far below the three-fold range of L_{200} observed across diverse sets of celluloses from higher plants (Newman 1999; Driemeier and Bragatto 2013). More important for the present work, such a percentage is considerable below the $\approx$40 % increase in lateral dimensions due to hydrothermal treatments (2.9 $\rightarrow$ 3.9 nm for L_{200}; 2.4 $\rightarrow$ 3.5 nm for $L_{1\bar{1}0}$ and L_{110}; see Fig. 6). Therefore, increasing crystallite mean lateral dimensions seems to be a necessary main part of the interpretation of sharper equatorial diffraction peaks.

The next question concerns *how* crystallite lateral dimensions increase. An *accretion* mechanism would require amorphous cellulose surrounding crystallites in raw bagasse and crystallization of this amorphous upon hydrothermal treatment, expanding existing crystallites. We reject such accretion mechanism because it requires substantial amorphous cellulose in raw bagasse. Up to $\approx$40 % increase in crystallite lateral dimensions (Fig. 6) implies up to doubling ($1.4^2 \approx 2$) of crystallite cross-section area. Hence, accretion would require about half of the cellulose of raw bagasse to be amorphous, which is inconsistent with the fully crystalline cellulose inferred from Fig. 8. Therefore, increasing mean lateral dimensions of crystallites must result from interaction of *multiple* crystallites, which would be termed *co-crystallization* according to our definition.

Possible mechanisms of co-crystallization

Interaction of multiple adjacent crystallites rely on existence of crystallite aggregates (Hult et al. 2001; Fahlén and Salmén 2005; Driemeier and Bragatto 2013; Ding et al. 2014), which some authors denominate macrofibrils (Ding et al. 2014). In general, crystallites may aggregate with distinct crystallographic orientations, either with or without non-cellulosic spacers. For the denominations employed in this study, *aggregation* preserves original individuality of cellulose crystallites and, therefore, aggregation is not observable by XRD. On the other hand, original crystallite individuality is lost in *co-crystallization*, with resulting changes observable by XRD.

Crystallite fusion is one mechanism consistent with our definition of co-crystallization. In fusion, multiple laterally adjacent crystallites have to come into identical crystallographic orientation and match the bonds at crystallite interfaces, thus becoming a single crystallite larger than the initial ones. The possibility of crystallite fusion was recently supported by molecular dynamic simulations, which revealed high-temperature intercrystallite dehydration as a driver of fusion (Langan et al. 2014). Nevertheless, the

proposed *starting* model comprised aggregated cellulose crystallites with (1) perfect shape complementarity, (2) common crystallographic orientation, and (3) absence of non-cellulosic spacers (Langan et al. 2014). Although justifiable from the perspective of simulation, these simplified features (1–3) of the model from Langan et al. (2014) likely overestimated the tendency of fusion.

Migration of cellulose chains across crystallite interfaces might also produce results consistent with our definition of co-crystallization. Co-crystallization mechanism could be analogous to Ostwald ripening: thinner crystallites would lose chains until they vanish; wider crystallites would grow by gaining new chains; and minimization of surface area of crystallites would be the thermodynamic driver of the process. Nevertheless, so far no evidence has been provided, neither supporting nor rejecting such a chain migration mechanism in cellulosic biomass.

Experimental observations reported in this work are consistent with both crystallite fusion and chain migration mechanisms of co-crystallization. In addition to increasing crystallite lateral dimension, two links between mechanisms and observations are worth highlighting. First, co-crystallization is expected to have a statistical nature. This is supported by the observed increase in peak shape parameter p_{200} (Fig. 4), which, as mentioned, is consistent with increasing variability of crystallite size. Second, for co-crystallization critical role is played by compositional change, especially removal of hemicelluloses (see Figs. 2 and 6), although lignin removal and redistribution may also have a role (Sun et al. 2014b). Since hemicelluloses are thought to space crystallites apart from each other, hemicellulose removal would create direct contacts (i.e., free of non-cellulosic spacers) between aggregated crystallites. Beyond hydrothermal treatment early stages (i.e., at solubilization >5 %), such clearing of crystallite interfaces seems to be the limiting factor for co-crystallization.

Existence and location of disordered cellulose

As presented and discussed in "Degree of crystallinity" section, treated bagasse has x_{cr} below cellulose content (Fig. 8), indicating existence of a fraction of disordered (i.e., non-crystalline) cellulose, at least for the more severe treatment conditions. The nature and location of such disordered cellulose are questions that arise.

Our interpretation of this result follows the reasoning from a previous work of our group (Driemeier and Bragatto 2013). In that work we used precise measurements of monolayer hydration to estimate amount of disorder across wide set of celluloses isolated from higher plants, having cellulose I phase and variable amounts of residual hemicelluloses. We found that monolayer hydration is primarily explained by lateral dimensions of cellulose crystallites ($R^2 = 0.98$), while contents of hemicelluloses have secondary effect. From this result we proposed that disorder is inherent to interfaces of aggregated cellulose crystallites, no matter if such interfaces are populated by hemicelluloses or by cellulose itself. Inherent interfacial disorder may be though as a transition layer between contradictory crystallographic orientations in laterally adjacent, interfacing crystallites.

Hence, for interpretation of results of the present work, we propose that, in raw bagasse, hemicelluloses primarily play the role of inherent intercrystallite interfacial disorder. Once hemicelluloses are removed by hydrothermal treatment, a fraction of cellulose would be de-crystallized to play this structural role. In summary, in our interpretation of structural evolution due to hydrothermal treatments, hemicellulose removal (Fig. 2) promotes direct interfacing between cellulose crystallites, enabling (1) co-crystallization that results in larger crystallite lateral dimensions (Fig. 6) and (2) de-crystallization (Fig. 8) of cellulose fractions located in crystallite interface regions.

Conclusions

We investigated the evolution of cellulose crystallites in sugarcane bagasse submitted to wide range of hydrothermal treatments. Treatments were performed at 160–190 °C, solubilizing up to 50 % of the bagasse mass. Fine structure of crystallites was parameterized through CRAFS analysis of two-dimensional XRD patterns acquired in fiber and powder diffraction modes. We observed cellulose structural parameters changing progressively with solubilization promoted by treatments. At early treatment stages (<5 % solubilization), structural change occur without noticeable loss of hemicelluloses. At higher solubiliza-

tion, on the other hand, cellulose structural changes co-occur with changes in chemical composition, primarily solubilization of hemicelluloses.

In agreement with previous reports, we found that increasing crystallite mean lateral dimensions is a key structural modification promoted by hydrothermal treatments. With basis on our experimental observations, we argue that increasing crystallite lateral dimensions results from co-crystallization, which we define in terms of interaction of multiple aggregated crystallites. By removing non-cellulosic components, especially hemicelluloses acting as intercrystallite spacers, we propose that treatments promote direct contacts between aggregated cellulose crystallites. Co-crystallization and partial cellulose de-crystallization would result from such direct interfacing of cellulose crystallites. This proposition is consistent with the observation of cellulose structure changing concurrently to chemical composition in hydrothermally treated sugarcane bagasse.

Acknowledgments Authors acknowledge CNPq and FAPESP (Grants 10/05523-3 and 10/08691-4) for financial support and LNBio and LNLS for providing X-ray beam time (proposal GAR 15208).

References

Alvira P, Tomás-Pejó E, Ballesteros M, Negro MJ (2010) Pretreatment technologies for an efficient bioethanol production process based on enzymatic hydrolysis: a review. Bioresour Technol 101:4851–4861

Cheng G, Zhang X, Simmons B, Singh S (2014) Theory, practice and prospects of x-ray and neutron scattering for lignocellulosic biomass characterization: towards understanding biomass pretreatment. Energy Environ Sci 8:436–455

Cortez LAB (ed) (2010) Sugarcane bioethanol: R&D for productivity and sustainability. Blucher, São Paulo

Davidson TC, Newman RH, Ryan MJ (2004) Variations in the fibre repeat between samples of cellulose I from different sources. Carbohydr Res 339:2889–2893

Ding S-Y, Zhao S, Zeng Y (2014) Size, shape, and arrangement of native cellulose fibrils in maize cell walls. Cellulose 21:863–871

Driemeier C (2014) Two-dimensional Rietveld analysis of celluloses from higher plants. Cellulose 21:1065–1073

Driemeier C, Bragatto J (2013) Crystallite width determines monolayer hydration across a wide spectrum of celluloses isolated from plants. J Phys Chem B 117:415–421

Driemeier C, Calligaris GA (2011) Theoretical and experimental developments for accurate determination of crystallinity of cellulose I materials. J Appl Crystallogr 44:184–192

Driemeier C, Francisco LH (2014) X-ray diffraction from faulted cellulose I constructed with mixed Iα–Iβ stacking. Cellulose 21:3161–3169

Driemeier C, Santos WD, Buckeridge MS (2012) Cellulose crystals in fibrovascular bundles of sugarcane culms: orientation, size, distortion, and variability. Cellulose 19:1507–1515

Driemeier C, Pimenta MTB, Rocha GJM, Oliveira MM, Mello DB, Maziero P, Gonçalves AR (2011) Evolution of cellulose crystals during prehydrolysis and soda delignification of sugarcane lignocellulose. Cellulose 18:1509–1519

Fahlén J, Salmén L (2005) Pore and matrix distribution in the fiber wall revealed by atomic force microscopy and image analysis. Biomacromolecules 6:433–438

Foston M, Ragauskas AJ (2010) Changes in lignocellulosic supramolecular and ultrastructure during dilute acid pretreatment of Populus and switchgrass. Biomass Bioenergy 34:1885–1895

French AD (2014) Idealized powder diffraction patterns for cellulose polymorphs. Cellulose 21:885–896

Garrote G, Domínguez H, Parajo JC (1999) Hydrothermal processing of lignocellulosic materials. Holz als Roh- und Werkst 57:191–202

Gouveia ER, Nascimento RT, Souto-Maior AM, Rocha GJM (2009) Validação de metodologia para a caracterização química de bagaço de cana-de-açúcar. Quím Nova 32: 1500–1503

Hosemann R, Hindeleh AM (1995) Structure of crystalline and paracrystalline condensed matter. J Macromol Sci Part B Phys B34:327–356

Hult E-L, Larsson PT, Iversen T (2001) Cellulose fibril aggregation—an inherent property of kraft pulps. Polymer 42:3309–3314

Inagaki T, Siesler HW, Mitsui K, Tsuchikawa S (2010) Difference of the crystal structure of cellulose in wood after hydrothermal and aging degradation: a NIR spectroscopy and XRD study. Biomacromolecules 11:2300–2305

Inouye H, Zhang Y, Yang L, Venugopalan N, Fishetti RF, Gleber CS, Vogt S, Fowle W, Makowski B, Tucker M, Ciesielski P, Donohoe B, Matthews J, Himmel ME, Makowski L (2014) Multiscale deconstruction of molecular architecture in corn stover. Sci Rep 4:3756

Ioelovitch M (1992) Zur übermolekularen Struktur von nativen und isolierten Cellulosen. Acta Polym 43:110–113

Langan P, Petridis L, O'Neill HM, Pingali SV, Foston M, Nishiyama Y, Schulz R, Lindner B, Hanson BL, Harton S, Heller WT, Urban V, Evans BR, Gnanakaran S, Ragauskas AJ, Smith JC, Davison BH (2014) Common processes drive the thermochemical pretreatment of lignocellulosic biomass. Green Chem 16:63

Langford JI, Wilson AJC (1978) Scherrer after sixty years: a survey and some new results in the determination of crystallite size. J Appl Crystallogr 11:102–113

Leppänen K, Andersson S, Torkkeli M, Knaapila M, Kotelnikova N, Serimaa R (2009) Structure of cellulose and microcrystalline cellulose from various wood species, cotton and flax studied by X-ray scattering. Cellulose 16:999–1015

Mosier N, Wyman C, Dale B, Elander R, Lee YY, Holtzapple M, Ladisch M (2005) Features of promising technologies for pretreatment of lignocellulosic biomass. Bioresour Technol 96:673–686

Newman RH (1999) Estimation of the lateral dimensions of cellulose crystallites using 13C NMR signal strengths. Solid State Nucl Magn Reson 15:21–29

Nishiyama Y, Langan P, Chanzy H (2002) Crystal structure and hydrogen bonding system in cellulose Iβ from synchrotron X-ray and neutron fiber diffraction. J Am Chem Soc 124:9074–9082

Nishiyama Y, Langan P, O'Neill H, Pingali SV, Harton S (2014) Structural coarsening of aspen wood by hydrothermal pretreatment monitored by small- and wide-angle scattering of X-rays and neutrons on oriented specimens. Cellulose 21:1015–1024

Okano T, Koyanagi A (1986) Structural variation of native cellulose related to its source. Biopolymers 25:851–861

Oliveira RP, Driemeier C (2013) CRAFS: a model to analyze two-dimensional X-ray diffraction patterns of plant cellulose. J Appl Crystallogr 46:1196–1210

Penttilä PA, Kilpeläinen P, Tolonen L, Suuronen J-P, Sixta H, Willför S, Serimaa R (2013) Effects of pressurized hot water extraction on the nanoscale structure of birch sawdust. Cellulose 20:2335–2347

Pingali SV, O'Neill HM, Nishiyama Y, He L, Melnichenko YB, Urban V, Petridis L, Davison B, Langan P (2014) Morphological changes in the cellulose and lignin components of biomass occur at different stages during steam pretreatment. Cellulose 21:873–878

Polikarpov I, Perles LA, De Oliveira RT, Oliva G, Castellano EE, Garratt RC, Craievich A (1998) Set-up and experimental parameters of the protein crystallography beamline at the Brazilian National Synchrotron Laboratory. J Synchrotron Radiat 5:72–76

Roe R-J (2000) Methods of X-ray and neutron scattering in polymer science. Oxford University Press, New York

Ruiz HA, Rodríguez-Jasso RM, Fernandes BD, Vicente AA, Teixeira JÁ (2013) Hydrothermal processing, as an alternative for upgrading agriculture residues and marine biomass according to the biorefinery concept: a review. Renew Sustain Energy Rev 21:35–51

Sluiter A, Hames B, Ruiz R, Scarlata C, Sluiter J, Templeton D (2005) Determination of Ash in Biomass. Technical Report NREL/TP-510-42622

Sluiter A, Hames B, Ruiz R, Scarlata C, Sluiter J, Templeton D, Crocker D (2008) Determination of structural carbohydrates and lignin in biomass. Technical Report NREL/TP-510-42618

Sun Q, Foston M, Sawada D, Pingali SV, O'Neill HM, Li H, Wyman CE, Langan P, Pu Y, Ragauskas AJ (2014a) Comparison of changes in cellulose ultrastructure during different pretreatments of poplar. Cellulose 21:2419–2431

Sun Q, Foston M, Meng X, Sawada D, Pingali SV, O'Neill HM, Li H, Wyman CE, Langan P, Ragauskas AJ, Kumar R (2014b) Effect of lignin content on changes occurring in poplar cellulose ultrastructure during dilute acid pretreatment. Biotechnol Biofuels 7:150

Thomas LH, Altaner CM, Jarvis MC (2013) Identifying multiple forms of lateral disorder in cellulose fibres. J Appl Crystallogr 46:972–979

Wyman CE (ed) (2013) Aqueous pretreatment of plant biomass for biological and chemical conversion to fuels and chemicals. Wiley, Chichester